Structure Identification and Analysis in Turbulent Boundary Layers by Stereo PIV

E.K. Longmire, B. Ganapathisubramani, I. Marusic, T. Urness

Abstract Stereoscopic PIV was used to measure three instantaneous components of velocity in streamwise-spanwise planes of a turbulent boundary layer. The local boundary layer thickness was δ = 69 mm, and the corresponding Reynolds number based on friction velocity was 1060. Data sets were obtained in the log region at wall-normal positions of $z^+ = 92$ and $z^+ = 192$. The resulting velocity fields at $z^+ = 92$ revealed distinctive signatures of vortex packets similar to those observed by Adrian, Meinhart, & Tomkins (2000). At this height, trains of 'necks' from hairpin vortices were observed aligned with the streamwise direction. The packets, which were frequently associated with high levels of Reynolds stress, appear to be a dominant mechanism for near-wall momentum transport. At $z^+ = 192$, larger individual vortex cores and heads of hairpin vortices were observed, but packet structures within the plane were not as evident.

1 Introduction

Because of their importance in practical applications, turbulent boundary layers have been studied in great depth over the last 60 years. In terms of boundary layer characterization, an issue that remains is how to model boundary layer behavior at very high Reynolds numbers as would occur, for example, on aircraft and ship surfaces, and in environmental applications. Current models are typically based on experiments and numerical simulations carried out at much lower Reynolds numbers. In order to develop accurate physically-based models, it is important to understand the types of eddies that develop and evolve in the shear layer between the free stream and the wall. In the current study, we attempt to examine the structure of the logarithmic region of the boundary layer. In this region, both experimental and numerical studies have postulated and documented the existence of hairpin-like vortices inclined at an angle to the free stream (see, for example, Head and Bandyopadhyay, 1981, Panton, 1997, and Robinson, 1991) that are thought to be responsible for the generation of bursting and ejection events where slow moving fluid is lifted away from the wall. These events are thought to be strong contributors to the Reynolds stress within the boundary layer and consequently to surface drag. More recently, Adrian et al. (2000) have documented the existence of 'vortex packets' in turbulent boundary layers by performing planar PIV measurements in streamwise-wall-normal flow planes. The experimental results corresponded well with three-dimensional simulations (Zhou et al., 1999) examining the development and propagation of such packets. The existence of vortices organized within packets also helps explain the long tails on streamwise velocity autocorrelations within the boundary layer (see Townsend, 1976, and Marusic, 2001).

The objective of the current study is to apply Stereo PIV in streamwise-spanwise planes parallel with the wall to measure three-dimensional velocity fields and to develop methods for the identification of typical flow structures at different heights above the wall. These methods can then be applied to quantify the strength, size, and frequency of various structures and therefore to examine the existence, nature, and symmetry of hairpin-like vortices and vortex packets.

2 Facility and Methods

The measurements were carried out in a suction wind tunnel with working section of 0.33 m height, 1.22 m width and 4.8 m length. Measurement planes were located 3.3 m downstream of a trip wire in a zero-pressure-gradient flow with freestream velocity U_∞ = 5.9 m/s. Hot-wire measurements showed that the turbulence intensity in the freestream was less than 0.2%. The Reynolds number based on the momentum thickness Re_θ was 2500, and the Karman number Re_τ was 1060. The boundary layer thickness (δ) in the region of the measurement planes was 69 mm.

E.K. Longmire*, B. Ganapathisubramani*, I. Marusic*, T.Urness©
* : Department of Aerospace Engineering & Mechanics, University of Minnesota, Minneapolis, MN, USA
© :Department of Computer Science and Engineering , University of Minnesota, Minneapolis, MN, USA
Correspondence to:
E.K. Longmire, Department of Aerospace Engineering & Mechanics, 110 Union St, SE, University of Minnesota, Minneapolis, MN, 55455, USA,
E-mail: ellen@aem.umn.edu

This work was supported by the National Science Foundation under Grant ACI-9982274.

The flow was seeded with olive oil droplets (nominal diameter 1 μm) that were generated by 8 Laskin nozzle units set up in parallel. The oil droplets were ingested into the intake of the wind tunnel upstream of honeycomb straighteners and screens used for flow conditioning. At the test section, glass side-walls and a glass bottom wall were installed in the wind tunnel to provide high-quality optical access. The seed particles were illuminated by pulsed sheets from two Nd:YAG lasers (Big Sky CFR200) directed through one side window and oriented parallel with the bottom wall of the tunnel. (See Figure 1). The laser pulse energy was 150 mJ, and the thickness of each sheet was 0.15 mm. Sets of digital images were captured by two Kodak Megaplus dual-frame CCD cameras (1024 x 1024 pixels). A TSI synchronizer box was used to control the strobing and timing of the cameras and lasers.

The cameras were aligned in a plane parallel with the spanwise-wall-normal flow plane and inclined at angles of 15° to the wall-normal direction as shown in Figure 1. Since the object plane was not parallel to either lens plane, the perspective view caused a geometric distortion. To overcome this problem, the Scheimpflug condition that requires the object, the lens, and the image plane to intersect at a common line was enforced. This arrangement introduces strong perspective distortion and varied magnification across the image, requiring that the camera configuration be calibrated for each measurement location.

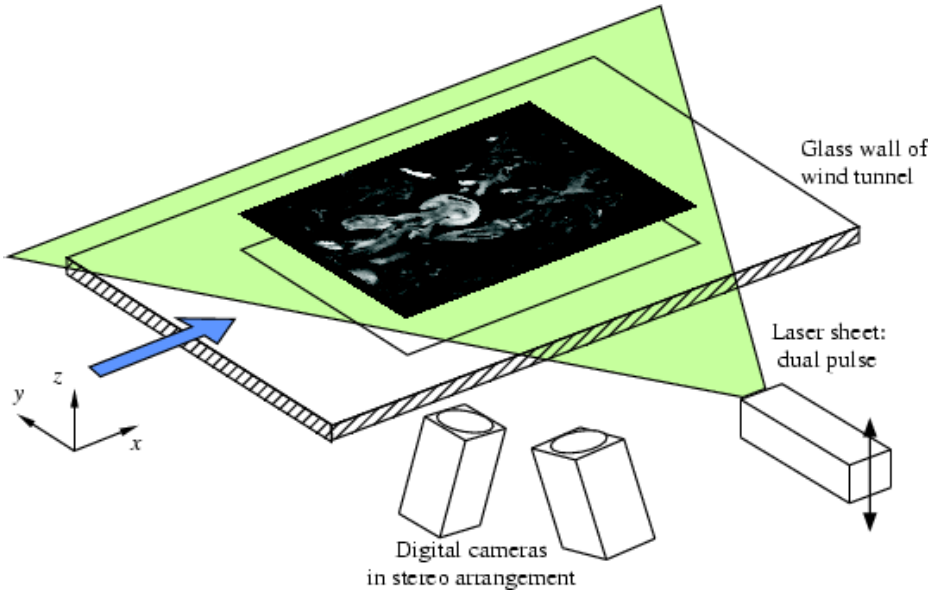

Figure 1: Experimental setup.

Each flow field was calibrated using a fixed plate located coincident with the eventual laser sheet plane. The plate was machined to contain fiducial marks in two planes parallel with and displaced on either side of the laser sheet by 0.5 mm. The image of the calibration target was captured by both cameras and analyzed with PIVcalib software from TSI. The software generated a calibration file with a set of mapping functions that relate the pixel locations in each image to the actual location in the laser sheet plane. The mapping functions were used to compute calibration coefficients for equations relating the pixel displacement in two directions (x and y) associated with each camera to the real displacements in the plane of the laser sheet. Hence, a set of four equations (dx,dy for each camera) with three unknowns (dX,dY,dZ, the actual displacements) was generated. When flow images were acquired for PIV, an in-plane cross correlation algorithm was employed to compute the pixel displacements for each camera. These pixel displacements were transformed into three-dimensional velocity vectors by solving the set of four equations in three unknowns using the least squares method. TSI Insight (3.2) software was used to compute pixel and fluid displacements. Additional details of the calibration and vector reconstruction schemes are given in Ganapathisubramani et al. (2001).

The images acquired covered an area of 1.2δ x 1.2δ with the overlap area (region in which the three components of the velocity field are computed) being 1.0δ x 1.0δ. Each data set consisted of 750 images captured at a rate of 15 Hz. The seeding particles had a nominal size of 2-3 pixels in diameter. The images were blurred to reduce the effect of noise and to eliminate pixel bias. To enhance the quality of the computed vector fields, interrogation spot windows in each image pair were offset by the mean pixel displacement of ~4 pixels while performing all cross correlations. For all derived quantities, the interrogation spot size used was 16 x 16 pixels (1 mm = 15 wall units) with 50 % overlap. In the figures, vectors resulting from 32 x 32 pixel interrogation spots with 50% overlap are plotted. We also employed an iterative algorithm using a 32 x 32 window as a predictor to compute vectors from 4

x 4 pixel areas (~4 wall units) in order to resolve smaller scales in the flow. As this paper focuses on larger-scale structures, these results are not presented below.

The measurements had two major sources of uncertainty. First, the Gaussian peak fit in the cross-correlation algorithm generated an uncertainty of approximately 0.1 pixels. Second, a residual error arises due to the least square curve fit in solving the four pixel-displacement equations in three unknowns. This residual error can play a major role in the uncertainty if concentration gradients in seeding occur within the flow field. In this experiment, such gradients were not significant, and this error was on average about half of the Gaussian error. A maximum value of 0.2 pixels was observed.

Velocity gradients were computed on each reconstructed vector grid using a second order central difference scheme wherever possible in the domain and a first order forward or backward difference at the boundaries. To identify the swirling motion or the eddies in the flow field, we use a quantity called the swirl strength λ_{ci} (Zhou et al., 1999) which is the magnitude of the imaginary part of the eigenvalue of the local velocity gradient tensor. Since the PIV images are planar, we use only the in-plane gradients and form a two dimensional form of the tensor. Vortices can be identified by extracting iso-regions of λ_{ci} (Adrian, Christensen & Liu, 2000). All quantities in the figures are normalized using the wall-shear velocity U_τ and the kinematic viscosity ν.

Several strategies were attempted in order to identify hairpin-like structures and packets. In the results presented, a dual-threshold method was first employed to identify regions of strong positive or negative wall-normal vorticity. In this case, each image was searched for all locations where the vorticity magnitude exceeded two standard deviations. Then, vorticity 'patches' were identified by first requiring at least 7 neighboring points that exceeded the threshold, and then including all connected pixels that exceeded a relaxed threshold within 13% of the original one. After, vortical regions were identified, an additional search was performed for regions of relatively low streamwise velocity between the regions of strong negative and positive vorticity. In the figures shown in the next section, low streamwise velocity was defined as 5% less than the global mean at the given wall-normal position. An additional requirement for the low velocity regions was that at least 10 neighboring points must fall below the specified threshold. The threshold values chosen above are somewhat arbitrary and have not been optimized systematically.

3 Results

In all plots shown, the streamwise, spanwise, and wall-normal directions are represented by x, y, and z respectively, and the corresponding velocity components are given by u, v, and w. Positive w is directed away from the wall. Sample plots from an instantaneous flow field where the local mean velocity ($U_c = 0.65U_\infty$) has been subtracted are given in Figure 2. The measurement plane is located at $z/\delta = 0.09$ ($z^+ = 92$), which falls within the logarithmic region. In Figure 2a-c respectively, the contour levels represent wall-normal vorticity, swirl strength, and kinematic Reynolds shear stress -u'w'. The velocity vectors and vorticity contours in Figure 2a show evidence of a variety of structures in the field. For example, the antisymmetric negative and positive vorticity contours at (x^+, y^+) = (600, 880) are indicative of the neck or legs of a single hairpin vortex. (To describe a hairpin vortex, we are using the nomenclature of Robinson, 1991). The longer streamwise region including streaks of opposing vorticity centered at (x^+, y^+) = (600, 380) are indicative of a vortex packet. Also, a long streamwise region of relatively high streamwise velocity crosses the field at $y^+ = 750$. Examination of the corresponding plot of swirl strength in Figure 2b reveals large values corresponding with vortex cores (as opposed to shearing zones) which occur at the location of the single hairpin mentioned above as well as on opposite spanwise sides of the vortex packet. The streaming zone with relatively large streamwise velocity does not contain strong cores. The plot of Reynolds shear stress in Figure 2c highlights (with blue and green) areas of slow-moving fluid directed away from the wall as well as areas of faster-moving fluid directed toward the wall. Note that all three of the zones mentioned above contain strongly negative values of u'w'. A separate plot of wall-normal velocity (not shown) reveals significant upflow inside of the single hairpin, strong upflow within the packet, and areas of downflow in the streaming zone. The extended zone within the vortex packet contains particularly large values of Reynolds stress (up to $u'w'/U_\tau^2 = -22$) due to the local combination of strong negative u' and strong positive w' that must result from the combined induction of the multiple vortices within the packet.

Figure 2d demonstrates the structure identification algorithm described above, where strong vortical regions are marked with deep blue and red, and regions of low streamwise velocity between them are marked with green. The large packet is identified effectively by this algorithm, but a second smaller green area (which requires neighboring blue and red areas of strong vorticity) is also identified. The smaller green zone is associated with flow between a single pair of cores as might occur in a single structure, as opposed to flow through a series of cores. It is interesting to observe, however, that this core falls within a skewed streamwise series stretching from the upper right corner of Figure 2a to $x^+ \approx 400$. This series may represent part of a 'looser' packet.

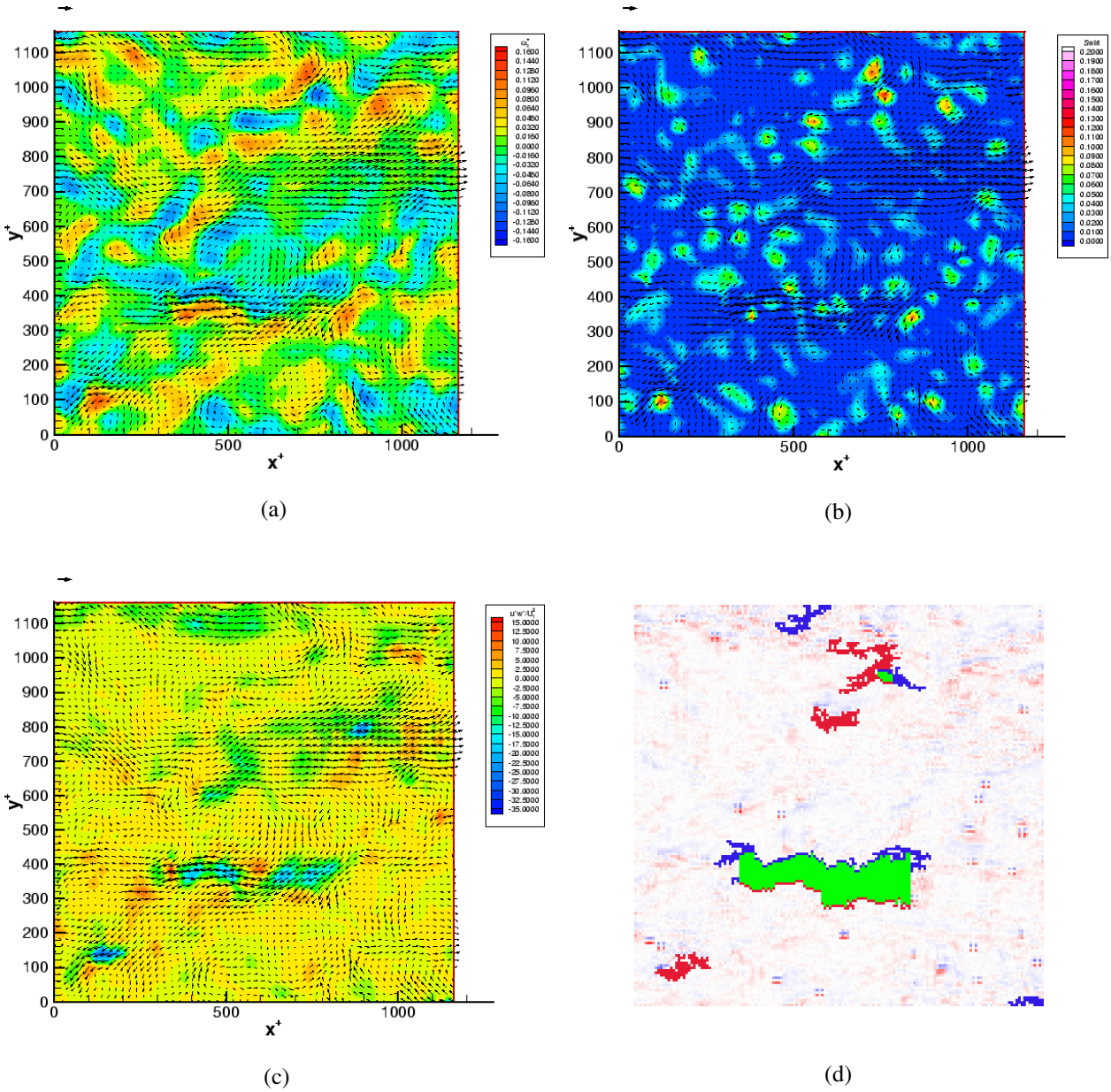

Figure 2. Streamwise-spanwise plane at $z^+ = 92$: (a) vorticity, (b) swirl strength, (c) u'w', (d) identified 'patches'.

At this height in the boundary layer, the types of structures described above ('necks' of single hairpins, vortex packets, and relatively long streamwise zones of high or low streamwise velocity) occur in most of the images examined. Vortex packets have varying lengths as well as varying number of cores that are identifiable. These results can be caused both by actual variations in packet length and by variations in inclination angle of the packets, i.e. long packets with significant inclination may appear relatively short in the streamwise-spanwise cuts examined. (Refer to Adrian et al., 2000 for streamwise-wall-normal views of vortex packets, almost all of which have significant inclination angles).

A series of plots for a separate flow field is shown in Figure 3. In this instance, it appears that a single skewed packet may extend across the entire streamwise field of view. (Note the vortical structures extending along the line connecting $(x^+, y^+) = (1100, 600)$ to $(x^+, y^+) = (0, 0)$). As in the previous field shown, the packet generates large values of Reynolds shear stress through its spanwise center (see the left half of Figure 3c), and the small streamwise velocity in that zone is found by the structure identification algorithm (Figure 3d). The vorticity levels in the downstream half of the packet did not exceed the threshold values in the algorithm, and therefore they are not marked in the plot. The algorithm does find another shorter packet beside the stronger, longer one.

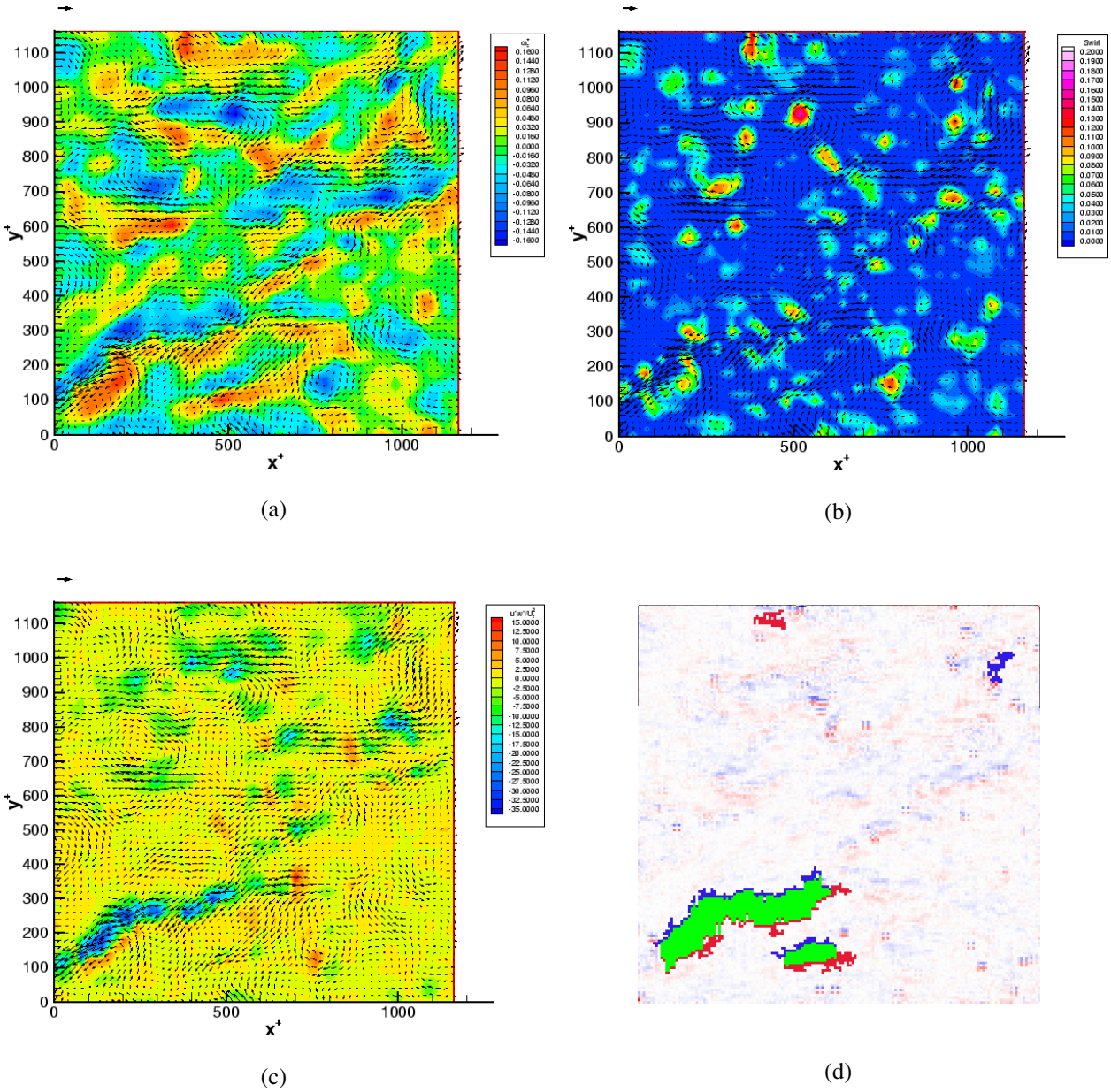

Figure 3. Streamwise-spanwise plane at $z^+ = 92$: (a) vorticity, (b) swirl strength, (c) u'w', (d) identified 'patches'.

It is interesting to observe the position and strength of the vortex cores located along the packets. Sometimes cores with similar strength and opposite vorticity are located directly across from each other as would be expected in a symmetric hairpin with two legs. On the other hand, cores on opposite spanwise sides of the packet can vary in strength and position. These variations could be caused by tilting and skewing of hairpins that were originally relatively symmetric. In this figure and others (see the two long streamwise packets shown in Figure 4 near $y^+ =$ 200 and 540) the typical spacing between 'neck' cores in packets is on the order of 100 wall units.

Results were also obtained at a wall-normal position of $z^+ = 192$ ($z/\delta = 0.18$); this corresponds nominally to the edge of where the log region would apply. At this wall-normal position, the flow structure appeared much less organized in that coherent 'packets' of vortices were not obvious. There are two possible causes for this result. First, packets extending to this wall-normal position are typically inclined, and most of the packet structure lies beneath the plane. Second, hairpins that extend outwards of this position are more likely to have necks and legs that are tilted and skewed so that their signatures are less clear. The vorticity plot in Figure 5 shows a pattern that is possibly associated with a series of hairpins (see the region surrounding (x^+, y^+) = (1100, 500)). In this case, it is possible that some of the neck cores are wrapping around one another.

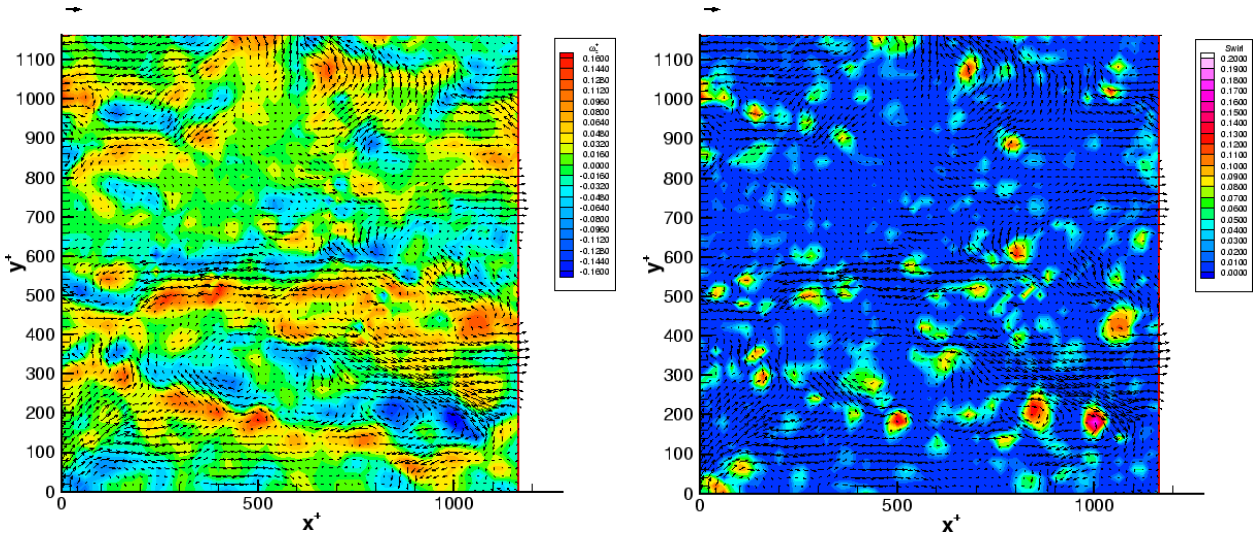

(a) (b)

Figure 4. Streamwise-spanwise plane at $z^+ = 92$: (a) vorticity, (b) swirl strength.

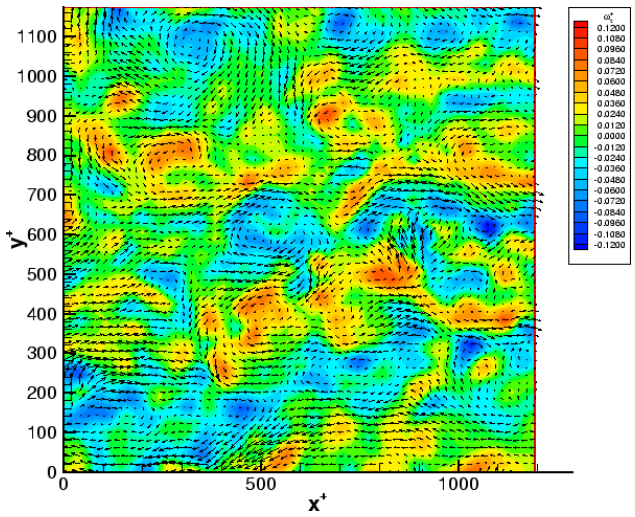

Figure 5. Streamwise-spanwise plane at $z^+ = 192$: vorticity.

The observance of reduced spatial coherence at positions at the edge and outside of the log region is consistent with the attached eddy modeling study of Marusic (2001). In the attached eddy formulation, the kinematic state of the boundary layer is modeled by a statistical ensemble of coherent vortex structures distributed across a range of length and velocity scales with varying population density across the length scales. From this formulation, predictions are made of two-point velocity correlations and other statistics. Marusic found that, for positions in the log region, a packet of hairpin vortices was needed in order for the correlations to agree with experiments. However, this spatial coherence was not needed for the outer part of the boundary layer beyond the log region. There, adequate results were obtained with single hairpin vortices that are uncorrelated with other eddies.

Figure 6a,b shows a separate field at $z^+ = 192$ with several interesting features. First, notice the large upwash zone near the center left of the field in the plot of wall-normal velocity (Figure 6b). This region has a spanwise width on the order of 300 wall units that is wider than any coherent structure observed at $z^+ = 92$. Second, notice the large single vortex core centered at $(x^+, y^+) = (1100, 900)$ in Figure 6a. Individual cores like this appear commonly at this wall-normal location. Finally, note the spanwise strips of vorticity with alternating sign in the lower, right corner of Figure 6a. The spanwise scale of the strips (200 wall units) and the sense of vorticity suggest the presence of two hairpin heads. Signatures like these occur in additional fields at both wall-normal locations examined.

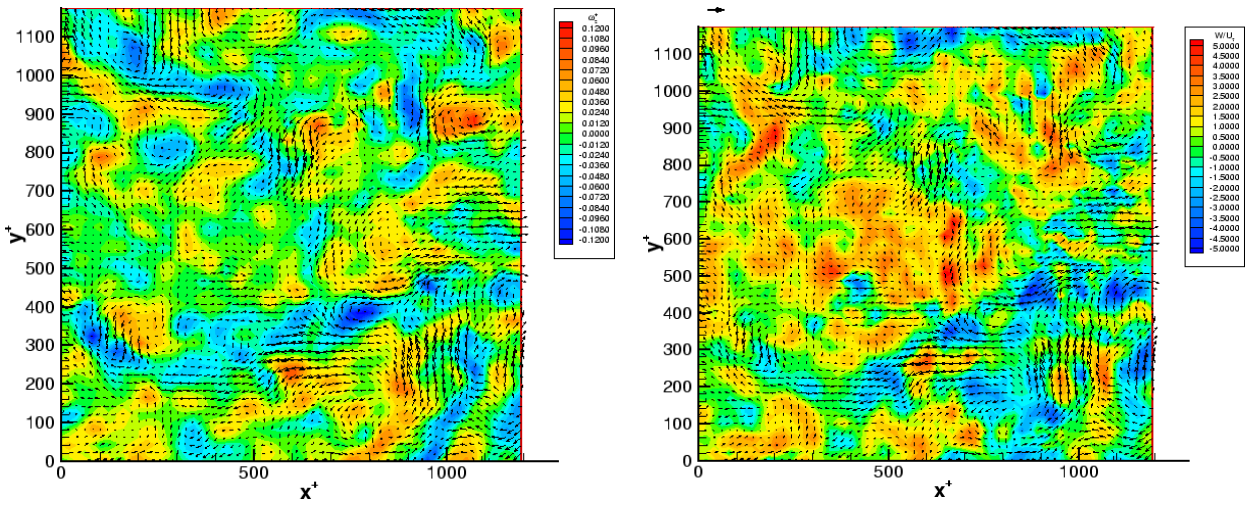

(a) (b)

Figure 6. Streamwise-spanwise plane at $z^+ = 192$: (a) vorticity, (b) wall-normal velocity 'w'.

4 Conclusions

In this paper, we have presented results of stereo PIV measurements in streamwise-spanwise planes of a turbulent boundary layer. The velocity fields and corresponding derived gradient quantities give an idea of the types of structures intersecting and crossing through different heights in the logarithmic region. At a height of $z^+ = 92$, packets of hairpin vortices, identified as streamwise series of neck structures, and long streamwise zones of relatively uniform streamwise velocity occurred fairly frequently. The zones of high streamwise velocity were typically free of structures with strong wall-normal vorticity. At a height of $z^+ = 192$, length scales of vortical structures with components normal to the measurement plane were larger, and packets were difficult to observe.

An algorithm for structure identification was presented that searched for regions containing streamwise strips of strong wall-normal vorticity of two signs and low streamwise velocity. The algorithm was implemented on a set of 750 flow fields at $z^+ = 92$ in order to identify vortex packets. It was found that the algorithm did a good job at identifying many packets, but it also identified smaller regions associated with single vortices. In addition, it missed portions of some packets and did not identify other packets at all. Currently, we are working on improving the sophistication of the identification algorithm in order to improve its performance.

5 References

Adrian, R.J.; Christensen, K.T.; Liu, Z.-C. (2000) Analysis and Interpretation of Instantaneous turbulent velocity fields, Exp Fluids, 29, 275-290.

Adrian, R.J.; Meinhart, C.D.; Tomkins, C.D. (2000) Vortex organization in the outer region of the turbulent boundary layer, J. Fluid Mech., 422, 1-53.

Ganapathisubramani, B.; Loyer, A.; Longmire, E.K.; Marusic, I. (2001) Three-dimensionality in the near field of a round jet, 2nd International Symposium on Turbulence and Shear Flow Phenomena, Stockholm.

Head, M.R.; Bandyopadhyay, P. (1981) New aspects of turbulent structure. J. Fluid Mech., 107, 297.

Marusic, I. (2001) On the role of large scale structures in wall turbulence, Phys. Fluids, 13, 735-743.

Panton, R.L. (1997) Self-Sustaining Mechanisms of Wall Turbulence. Comp. Mech. Publications, Southampton.

Robinson, S.K. (1991) Coherent motion in the turbulent boundary layer. Ann. Rev. Fluid Mech., 23, 601.

Townsend, A.A (1976) Structure of the turbulent boundary layer. Cambridge University Press, Cambridge, Vol 2.

Zhou, J.; Adrian, R.J.; Balachandar, S.; Kendall, T.M. (1999) Mechanisms for generating coherent packets of hairpin vortices in channel flow. J. Fluid Mech., 387, 353-359.